JACS
JOURNAL OF THE AMERICAN CHEMICAL SOCIETY
Communication
Cite This: J. Am. Chem. Soc. 2019, 141, 5078−5082
pubs.acs.org/JACS

Direct Observation of the Relationship between Molecular Topology and Bulk Morphology for a π-Conjugated Material

Martin T. Seifrid,[†] G. N. Manjunatha Reddy,[‡] Cheng Zhou,[†] Bradley F. Chmelka,*[,‡] and Guillermo C. Bazan*[,†]

[†]Center for Polymers and Organic Solids, Department of Chemistry and Biochemistry, University of California, Santa Barbara, Santa Barbara, California 93106, United States

[‡]Department of Chemical Engineering, University of California, Santa Barbara, Santa Barbara, California 93106, United States

Supporting Information

ABSTRACT: High-performance organic semiconducting materials are reliant upon subtle changes in structure across different length scales. These morphological features control relevant physical properties and ultimately device performance. By combining *in situ* NMR spectroscopy and theoretical calculations, the conjugated small molecule TT is shown to exhibit distinct temperature-dependent local structural features that are related to macroscopic properties. Specifically, lamellar and melt states are shown to exhibit different molecular topologies associated with planar and twisted conformations of TT, respectively. This topological transformation offers a novel avenue for molecular design and control of solid-state organization.

That form follows function is a central principle for the design of organic semiconductors (OSCs). Molecular shape[1,2] directly impacts solid-state organization and the kinetic profiles for achieving organized structures from solution.[3,4] The distances and orientations between subunits within thin films dictate electronic and optical properties[5,6] and thereby the applicability of a given material in emerging optoelectronic applications.[7,8] These considerations are relevant within the context of potential OSC implementation in new classes of lightweight, low-cost and solution-processable technologies such as photovoltaics,[9−13] thermoelectrics,[14,15] thin-film transistors,[16−19] light-emitting devices,[20−22] photodetectors[23] and various types of sensors.[24−27]

In OSC systems with internal modes of reconfiguration, insight into molecular shape is typically attained through single crystal X-ray analysis.[28,29] Information related to the shape and solid-state organization of amorphous systems, which represent an important fraction of materials used in the fabrication organic light-emitting diodes,[30] is currently out of reach. Molecular topology is important as it relates to crystallization of OSCs, especially those which are described by an awkward shape resistant to crystallization.

Understanding both intra- and supramolecular organizations, such as those related to the transformations exhibited by TT, and how they relate to each other would be useful for further refinement of molecular designs as they relate to maximizing solubility and solid-state organization. While experiments such as transmission electron microscopy (TEM) or X-ray scattering provide important information about organization in the bulk, they may be limited by the degree of disorder often present in OSCs. TEM can be used to identify various textures within the solid, but resolution at the molecular scale is typically unattainable due to the inherent disorder of solution-processable OSC materials.[31−33] X-ray scattering techniques provide information on molecular order, but are predominantly limited to probing the ordered regions of a solid.[34,35] Aside from certain exceptional cases,[36] *in situ* determination of molecular shape in the solid-state remains elusive.

The molecular OSC TT (Scheme 1 and Figure 2) is a relevant system to study. TT displays unusual behavior during its transition from solution to the solid-state.[37] Following film formation, the bulk initially forms an amorphous glass, which slowly transitions into a crystalline film, of which there are two polymorphs. This behavior of TT has been attributed to features of its molecular structure, specifically the central tail-to-tail coupled 3,3′-hexylbithiophene donor core. The extra degrees of conformational freedom, compared to traditional covalently rigidified electron-donating units, such as cyclopentadithiophene, give rise to better solubility. It has been proposed that the slow crystallization of TT involves planarization of the internal 3,3′-hexylbithiophene donor core, which involves a ∼7 kcal/mol energetic barrier according to theoretical calculations. Characterization of TT thin films via grazing incidence wide-angle X-ray scattering (GIWAXS)

Scheme 1. TT Has Been Proposed to Twist and Adopt a *trans*-Planar Conformation upon Crystallization[a]

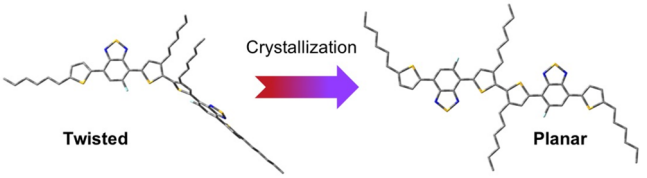

[a]Structures are the optimized ground-state equilibrium geometries from density functional theory (DFT) calculations. Hydrogen atoms were removed for clarity.

Received: December 10, 2018
Published: February 22, 2019

DOI: 10.1021/jacs.8b13200
J. Am. Chem. Soc. 2019, 141, 5078−5082

confirms that TT is amorphous in the melt and ordered in the solid. GIWAXS diffraction patterns of TT in the melt do not present any peaks, indicating a lack of long-range order. The diffraction pattern of TT in the ordered high-temperature state has a variety of scattering peaks, characteristic of lamellar and $\pi-\pi$ stacking. The relatively large number of diffraction peaks also indicates good intermolecular order. However, due to the superposition of two dimensions in GIWAXS experiments, direct determination of the arrangement of molecules within the unit cell is impossible.

In this contribution, we illustrate how to address this challenge through the use of solid-state magic-angle spinning (MAS) nuclear magnetic resonance spectroscopy (ssNMR) measurements. These techniques have been used to characterize the shapes of proteins, lipids and other biological structures,[38,39] as well as to understand molecular assembly and disassembly pathways during transitions between solution and solid-state.[40] Their application to OSCs has been relatively limited, such as to distinguish between ordered and disordered regions, and to characterize interfacial structures.[41−45] Here we examine topological differences at the molecular scale that exist in the melt and ordered states of TT. This characterization is accomplished by tracking changes in ^{13}C chemical shifts and the relative displacements of signals between the amorphous and ordered phases. ^{13}C MAS NMR spectra are analyzed in conjunction with DFT calculations to unravel that crystallization of TT requires twisting of the dihedral between the central thiophene rings from ∼112° to a *trans*-planar conformation.

The absorbance of TT changes between the solution and thin film states, as reproduced in Figure 1.[37] Immediately

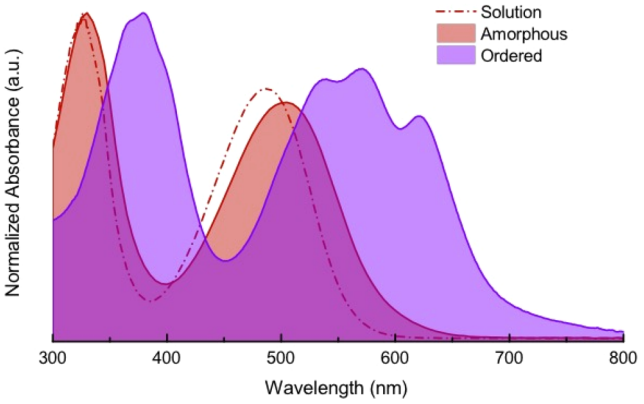

Figure 1. In its ordered state, the optical absorbance of TT is noticeably red-shifted relative to those of the amorphous and solution states. The optical absorbances of the solution and amorphous state are very similar, suggesting a similar degree of electronic delocalization along the conjugated backbone.

following spin-coating, the absorbance of the film is similar to that of the solution. The absorbance then shows a significant red-shift, which is fully reversible by heating and cooling the film past its melting point.[37] The resemblance of TT absorbance spectra in solution and the melt together with the observed red-shift in ordered lattices have been invoked to suggest planarization of the TT molecule.

Planarization of TT is expected to result in the greatest change in the chemical shifts from the two central-most ^{13}C nuclei (Figure 2, purple and yellow dots). Assignments of the signals observed in solution were first performed by analyzing

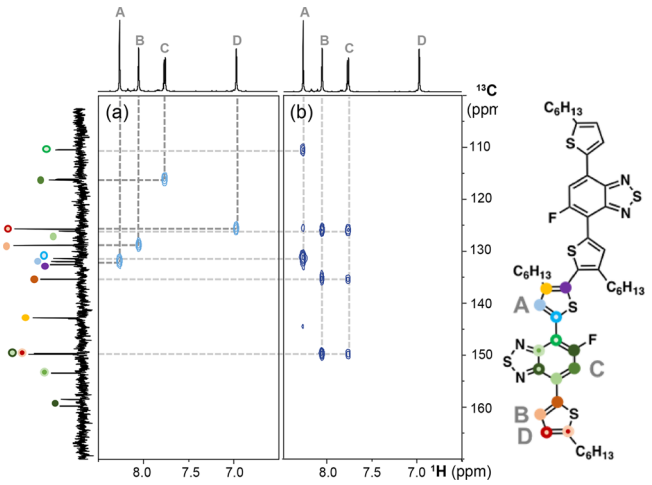

Figure 2. Solution-state 2D $^{1}H\{^{13}C\}$ HMBC spectra of the aromatic region of TT, acquired using contact times of (a) 3.4 ms and (b) 250 ms, enable isotropic ^{1}H and ^{13}C chemical shifts to be correlated for pairs of *J*-coupled nuclei. The schematic diagram of TT shows ^{13}C moieties assigned according to the colored labels in the left vertical spectrum, and ^{1}H moieties A-D as labeled in the top horizontal spectrum. Dashed gray lines serve as guides to the eye for correlations determined from (a) (dark gray) and (b) (light gray).

1D ^{1}H and ^{13}C NMR spectra (Figure S1), 2D $^{1}H\{^{1}H\}$ correlation (Figure S2) and $^{1}H\{^{13}C\}$ heteronuclear multiple-bond correlation (HMBC) NMR spectra (Figures 2 and S2). Complete details can be found in the Supporting Information.

The NMR spectroscopic features of TT in the melt are narrow and well resolved (Figure 3a). The amorphous state was achieved by heating the sample to 135 °C (above the melting point, 124 °C) under a stream of N_2 gas. Signal assignments are straightforward due to the similarity to what is observed in solution (Figure S3). As seen in Figure 3a, signals of greatest interest are located at 132.3 ppm (7, purple dot) and 141.7 ppm (5, yellow dot).

At 118 °C a single lamellar phase is observed,[37] in which the alkyl side chains are highly mobile and liquid-like[46,47] on the NMR time scale (ca. 10^{-5} s). This feature is supported by comparison of the ^{13}C CP-MAS NMR spectrum in Figure 3b with a static single-pulse ^{13}C NMR spectrum acquired under otherwise identical conditions (Figure S4); the latter exhibits broad spectral features in the aromatic region (120−165 ppm) that manifest relatively immobile $\pi-\pi$ stacked backbones and much narrower signals in the alkyl region (10−30 ppm) from mobile alkyl side chains. Analogous molecular- and mesoscale characteristics have been observed in lamellar silicate-surfactant phases with stiff covalently cross-linked silicate nanosheets separated by mobile alkyl surfactant chains.[48] Comparison of the 1D ^{13}C spectra (Figure 3) of the melt and lamellar phases reveals differences in the isotropic ^{13}C chemical shifts of the TT backbones, depending on whether they are amorphous versus aggregated into $\pi-\pi$ stacks. In particular, ^{13}C signals 5 and 7 are displaced in different directions from 141.7 to 139.8 ppm (yellow arrow) and from 132.3 to 139.8 ppm (purple arrow), respectively. Though these two signals overlap at 118 °C, a quantitative 1D ^{13}C MAS spectrum of TT (Figure S5) and separate DFT calculations (discussed below) corroborate their assignments. This is further supported by 2D $^{13}C\{^{1}H\}$ heteronuclear correlation (HETCOR) spectra acquired with different CP contact times (Figure S6), in

DOI: 10.1021/jacs.8b13200
J. Am. Chem. Soc. 2019, 141, 5078−5082

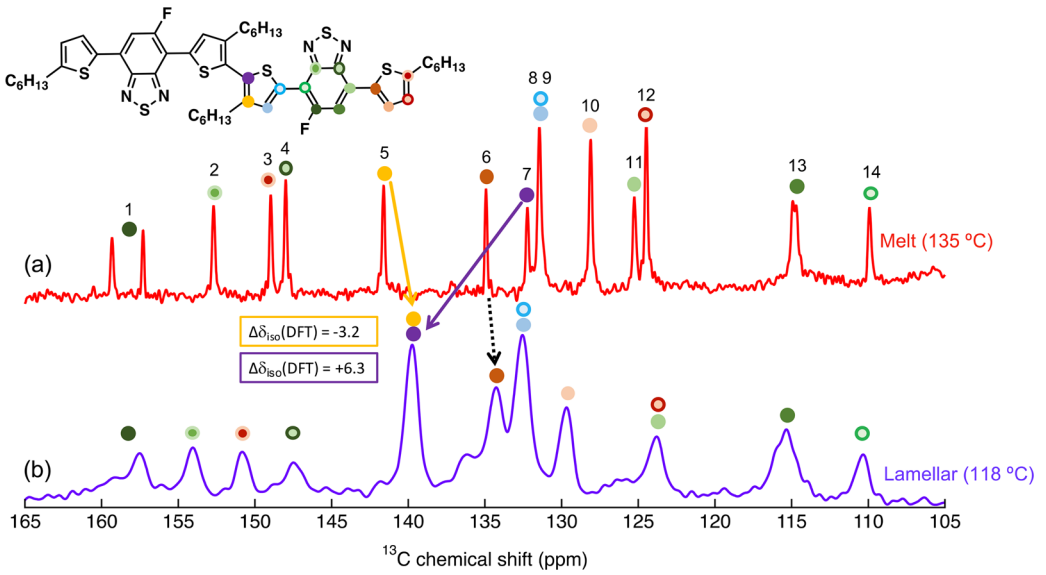

Figure 3. Aromatic regions of (a) the static single-pulse ^{13}C NMR spectrum of the melt state at 135 °C and (b) the ^{13}C{^{1}H} CP-MAS NMR spectrum of the lamellar phase at 118 °C. Displacements of the respective ^{13}C isotropic chemical shifts between panels a and b suggest different topologies of TT in the two states associated with different conformations or extents of $\pi-\pi$ stacking of the conjugated backbones. The color-coded ^{13}C signal assignments are the same as shown in Figure 2.

which the intramolecular ^{13}C−^{1}H proximities of carbon atoms 5 and 7 are distinguished from their peripheral counterparts (6 and 12).

The NMR analysis to this point yields little direct information regarding molecular topology. However, in combination with DFT modeling, the experimental isotropic ^{13}C chemical shifts associated with the melt and lamellar TT structures can be compared with DFT-calculated ^{13}C shieldings for twisted and planar TT backbone conformations (Scheme 1). The gauge-independent atomic orbital method of DFT was used with the semiempirically tuned ωB97XD functional and 6-311+G(2d,p) basis set.[49] The dielectric environment of an OSC is modeled with the conductor-like polarizable continuum model with the static dielectric constant as ε = 3.5 and the dynamic dielectric constant as ε_{inf} = 2.[50,51] Full details of the methods are given in the Supporting Information. Regression analyses were carried out by comparing experimental ^{13}C chemical shifts against the DFT-calculated ^{13}C shieldings for the twisted and planar conformers of TT (Figure S7).[52−55] Comparison of the experimental ^{13}C chemical shifts in the melt and ^{13}C shieldings of the twisted conformer of TT resulted in a regression coefficient of R^2 = 0.98. A similar analysis and comparison for the lamellar phase and ^{13}C shieldings of the planar conformer of TT resulted in R^2 = 0.99. Within the resolution limits of the NMR data and the validities of model assumptions, the level of agreement is noteworthy. Further accuracy in the calculation of chemical shieldings requires taking into account intermolecular contacts[56] that are not possible to model for an isolated molecule. This approach is also restricted to materials whose NMR spectra do not contain an excessive number of overlapping signals, which may be difficult to clearly resolve.

Differences in the experimental isotropic ^{13}C chemical shifts of the TT backbone between the melt and lamellar phases ($\Delta\delta_{iso}$ Expt., Figure 4) are also correlated to differences in molecular conformation and shape. We focus on the differences in DFT-calculated ^{13}C chemical shifts ($\Delta\delta_{iso}$ DFT) between the twisted and planar conformers. While

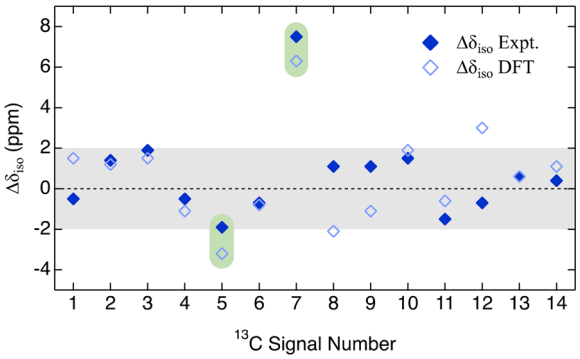

Figure 4. Relative differences in isotropic ^{13}C chemical shifts ($\Delta\delta_{iso}$) of the TT backbone nuclei between the melt and lamellar phases, as determined by high temperature ^{13}C NMR and from DFT. Most signals differ by <2 ppm (gray band), while those from carbon atoms 5 and 7 (green bands) show more pronounced differences. The discrepancies associated with signals 8, 9 and 12 likely arise from differences in the orientations of the alkyl chains relative to the structures used for DFT calculations.

most $\Delta\delta_{iso}$ values are within ±2 ppm (Figure 4, gray region), the ^{13}C atoms of most interest (signals 5 and 7, highlighted in green) are predicted to be displaced by −3.2 ppm and +6.3 ppm, respectively, compared to experimental values of −1.9 ppm and +7.5 ppm. These results are consistent with changes of the TT backbone geometry involving a transition from twisted to *trans*-planar conformations. The ssNMR results and DFT calculations are also consistent with the observed differences in the optical properties of TT (Figure 1). As TT adopts a planar molecular topology, the degree of electronic delocalization increases.

The combination of *in situ* NMR with DFT-based modeling provides new molecular-level insights that manifest important topological changes that were previously only hypothesized based on differences in macroscopic optical properties. Specifically, the combined NMR+DFT approach identifies a twisted molecular topology of TT in the melt state, while the

DOI: 10.1021/jacs.8b13200
J. Am. Chem. Soc. 2019, 141, 5078−5082

molecule is found to adopt a planar topology in the lamellar phase. Refinement of these methods as they relate to solid-state structures of OSCs is likely to reveal further information regarding the impact of intramolecular features and long-range organization on processes, such as charge carrier generation or transport, which ultimately determine technological feasibility. For example, we envision that the techniques described in this work may be extended to probe the effects of polymer architecture on charge carrier mobility. In the case of TT, the energy cost for planarization is compensated by lattice interactions that decrease the free energy relative to the amorphous state. From a practical perspective, such considerations are expected to enable control of solid-state structural features at the level of molecular design, enabling device performance to be decoupled from processing conditions. Potential advantages of such materials include development of device active layers that can be processed through deposition methods that are not solvent-dependent.

■ ASSOCIATED CONTENT

Supporting Information

The Supporting Information is available free of charge on the ACS Publications website at DOI: 10.1021/jacs.8b13200.

Experimental details, NMR spectra, DFT results (PDF)

■ AUTHOR INFORMATION

Corresponding Authors

*bazan@chem.ucsb.edu

*bradc@engineering.ucsb.edu

ORCID

G. N. Manjunatha Reddy: 0000-0002-8283-2462

Bradley F. Chmelka: 0000-0002-4450-6949

Guillermo C. Bazan: 0000-0002-2537-0310

Notes

The authors declare no competing financial interest.

■ ACKNOWLEDGMENTS

Solution and solid-state NMR experiments were carried out at the Central Facilities of the UCSB Materials Research Laboratory supported by the MRSEC program of the U.S. NSF under award no. DMR-1720256, which is a member of the NSF-funded Materials Research Facilities Network (www.mrfn.org). We acknowledge support from the Center for Scientific Computing from the CNSI, MRL: an NSF MRSEC (DMR-1720256) and NSF CNS-1725797. This work was supported by the Department of the Navy, Office of Naval Research, Award Nos. N00014-14-1-0580 and N00014-16-1-2520. B.F.C. and G.N.M.R. gratefully acknowledge the financial support from Mitsubishi Chemical-Centre for Advanced Materials (MC-CAM).

■ REFERENCES

(1) Conboy, G.; Spencer, H. J.; Angioni, E.; Kanibolotsky, A. L.; Findlay, N. J.; Coles, S. J.; Wilson, C.; Pitak, M. B.; Risko, C.; Coropceanu, V.; Brédas, J.-L.; Skabara, P. J. To Bend or Not to Bend − Are Heteroatom Interactions within Conjugated Molecules Effective in Dictating Conformation and Planarity? *Mater. Horiz.* **2016**, *3* (4), 333−339.

(2) Liu, X.; Sun, Y.; Hsu, B. B. Y.; Lorbach, A.; Qi, L.; Heeger, A. J.; Bazan, G. C. Design and Properties of Intermediate-Sized Narrow Band-Gap Conjugated Molecules Relevant to Solution-Processed Organic Solar Cells. *J. Am. Chem. Soc.* **2014**, *136* (15), 5697−5708.

(3) Liu, X.; Burgers, M. A.; Hsu, B. B. Y.; Coughlin, J. E.; Perez, L. A.; Heeger, A. J.; Bazan, G. C. Molecular Orientation within Thin Films of Isomorphic Molecular Semiconductors. *RSC Adv.* **2015**, *5* (108), 89144−89148.

(4) Seifrid, M. T.; Oosterhout, S. D.; Toney, M. F.; Bazan, G. C. Kinetic Versus Thermodynamic Orientational Preferences for a Series of Isomorphic Molecular Semiconductors. *ACS Omega* **2018**, *3* (8), 10198−10204.

(5) Djurovich, P. I.; Mayo, E. I.; Forrest, S. R.; Thompson, M. E. Measurement of the Lowest Unoccupied Molecular Orbital Energies of Molecular Organic Semiconductors. *Org. Electron.* **2009**, *10* (3), 515−520.

(6) Roncali, J. Synthetic Principles for Bandgap Control in Linear π-Conjugated Systems. *Chem. Rev.* **1997**, *97* (1), 173−206.

(7) Mas-Torrent, M.; Rovira, C. Role of Molecular Order and Solid-State Structure in Organic Field-Effect Transistors. *Chem. Rev.* **2011**, *111* (8), 4833−4856.

(8) Bredas, J. L.; Calbert, J. P.; da Silva Filho, D. A.; Cornil, J. Organic Semiconductors: A Theoretical Characterization of the Basic Parameters Governing Charge Transport. *Proc. Natl. Acad. Sci. U. S. A.* **2002**, *99* (9), 5804−5809.

(9) Roncali, J.; Leriche, P.; Blanchard, P. Molecular Materials for Organic Photovoltaics: Small Is Beautiful. *Adv. Mater.* **2014**, *26* (23), 3821−3838.

(10) Li, G.; Zhu, R.; Yang, Y. Polymer Solar Cells. *Nat. Photonics* **2012**, *6*, 153−161.

(11) Zhou, H.; Yang, L.; You, W. Rational Design of High Performance Conjugated Polymers for Organic Solar Cells. *Macromolecules* **2012**, *45*, 607−632.

(12) Mazzio, K. A.; Luscombe, C. K. The Future of Organic Photovoltaics. *Chem. Soc. Rev.* **2015**, *44* (1), 78−90.

(13) He, Z.; Wu, H.; Cao, Y. Recent Advances in Polymer Solar Cells: Realization of High Device Performance by Incorporating Water/Alcohol-Soluble Conjugated Polymers as Electrode Buffer Layer. *Adv. Mater.* **2014**, *26* (7), 1006−1024.

(14) Russ, B.; Glaudell, A.; Urban, J. J.; Chabinyc, M. L.; Segalman, R. A. Organic Thermoelectric Materials for Energy Harvesting and Temperature Control. *Nature Reviews Materials* **2016**, *1*, 16050.

(15) Chen, Y.; Zhao, Y.; Liang, Z. Solution Processed Organic Thermoelectrics: Towards Flexible Thermoelectric Modules. *Energy Environ. Sci.* **2015**, *8*, 401−422.

(16) Sirringhaus, H. 25th Anniversary Article: Organic Field-Effect Transistors: The Path beyond Amorphous Silicon. *Adv. Mater.* **2014**, *26* (9), 1319−1335.

(17) Zhang, W.; Liu, Y.; Yu, G. Heteroatom Substituted Organic/Polymeric Semiconductors and Their Applications in Field-Effect Transistors. *Adv. Mater.* **2014**, *26* (40), 6898−6904.

(18) Bisri, S. Z.; Piliego, C.; Gao, J.; Loi, M. A. Outlook and Emerging Semiconducting Materials for Ambipolar Transistors. *Adv. Mater.* **2014**, *26* (8), 1176−1199.

(19) Biniek, L.; Schroeder, B. C.; Nielsen, C. B.; McCulloch, I. Recent Advances in High Mobility Donor−Acceptor Semiconducting Polymers. *J. Mater. Chem.* **2012**, *22* (30), 14803.

(20) Geffroy, B.; le Roy, P.; Prat, C. Organic Light-Emitting Diode (OLED) Technology: Materials, Devices and Display Technologies. *Polym. Int.* **2006**, *55* (6), 572−582.

(21) Bernius, M. T.; Inbasekaran, M.; O'Brien, J.; Wu, W. Progress with Light-Emitting Polymers. *Adv. Mater.* **2000**, *12* (23), 1737−1750.

(22) Reineke, S.; Lindner, F.; Schwartz, G.; Seidler, N.; Walzer, K.; Lüssem, B.; Leo, K. White Organic Light-Emitting Diodes with Fluorescent Tube Efficiency. *Nature* **2009**, *459* (7244), 234−238.

(23) Baeg, K. J.; Binda, M.; Natali, D.; Caironi, M.; Noh, Y. Y. Organic Light Detectors: Photodiodes and Phototransistors. *Adv. Mater.* **2013**, *25*, 4267−4295.

(24) Rivnay, J.; Owens, R. M.; Malliaras, G. G. The Rise of Organic Bioelectronics. *Chem. Mater.* **2014**, *26* (1), 679−685.

(25) Someya, T.; Bao, Z.; Malliaras, G. G. The Rise of Plastic Bioelectronics. *Nature* **2016**, *540*, 379−385.

DOI: 10.1021/jacs.8b13200
J. Am. Chem. Soc. 2019, 141, 5078−5082

(26) Inal, S.; Rivnay, J.; Suiu, A. O.; Malliaras, G. G.; McCulloch, I. Conjugated Polymers in Bioelectronics. *Acc. Chem. Res.* **2018**, *51* (6), 1368−1376.
(27) Hua, Q.; Sun, J.; Liu, H.; Bao, R.; Yu, R.; Zhai, J.; Pan, C.; Wang, Z. L. Skin-Inspired Highly Stretchable and Conformable Matrix Networks for Multifunctional Sensing. *Nat. Commun.* **2018**, *9* (1), 244.
(28) Van Der Poll, T. S.; Zhugayevych, A.; Chertkov, E.; Bakus, R. C.; Coughlin, J. E.; Teat, S. J.; Bazan, G. C.; Tretiak, S. Polymorphism of Crystalline Molecular Donors for Solution-Processed Organic Photovoltaics. *J. Phys. Chem. Lett.* **2014**, *5* (15), 2700−2704.
(29) Coughlin, J. E.; Zhugayevych, A.; Bakus, R. C.; van der Poll, T. S.; Welch, G. C.; Teat, S. J.; Bazan, G. C.; Tretiak, S. A Combined Experimental and Theoretical Study of Conformational Preferences of Molecular Semiconductors. *J. Phys. Chem. C* **2014**, *118* (29), 15610.
(30) Tao, Y.; Yang, C.; Qin, J. Organic Host Materials for Phosphorescent Organic Light-Emitting Diodes. *Chem. Soc. Rev.* **2011**, *40*, 2943−2970.
(31) Yang, X.; Loos, J.; Veenstra, S. C.; Verhees, W. J. H.; Wienk, M. M.; Kroon, J. M.; Michels, M. A. J.; Janssen, R. A. J. Nanoscale Morphology of High-Performance Polymer Solar Cells. *Nano Lett.* **2005**, *5* (4), 579−583.
(32) Brinkmann, M.; Rannou, P. Molecular Weight Dependence of Chain Packing and Semicrystalline Structure in Oriented Films of Regioregular Poly(3-Hexylthiophene)Revealed by High-Resolution Transmission Electron Microscopy. *Macromolecules* **2009**, *42* (4), 1125−1130.
(33) Takacs, C. J.; Treat, N. D.; Krämer, S.; Chen, Z.; Facchetti, A.; Chabinyc, M. L.; Heeger, A. J. Remarkable Order of a High-Performance Polymer. *Nano Lett.* **2013**, *13* (6), 2522−2527.
(34) Rivnay, J.; Mannsfeld, S. C. B.; Miller, C. E.; Salleo, A.; Toney, M. F. Quantitative Determination of Organic Semiconductor Microstructure from the Molecular to Device Scale. *Chem. Rev.* **2012**, *112*, 5488−5519.
(35) McNeill, C. R.; Ade, H. Soft X-Ray Characterisation of Organic Semiconductor Films. *J. Mater. Chem. C* **2013**, *1* (2), 187−201.
(36) Takacs, C. J.; Brady, M. A.; Treat, N. D.; Kramer, E. J.; Chabinyc, M. L. Quadrites and Crossed-Chain Crystal Structures in Polymer Semiconductors. *Nano Lett.* **2014**, *14* (6), 3096−3101.
(37) Zhou, C.; Cui, Q.; McDowell, C.; Seifrid, M.; Chen, X.; Brédas, J. L.; Wang, M.; Huang, F.; Bazan, G. C. Topological Transformation of π-Conjugated Molecules Reduces Resistance to Crystallization. *Angew. Chem., Int. Ed.* **2017**, *56* (32), 9318−9321.
(38) McDermott, A. Structure and Dynamics of Membrane Proteins by Magic Angle Spinning Solid-State NMR. *Annu. Rev. Biophys.* **2009**, *38* (1), 385−403.
(39) Tycko, R. Solid-State NMR Studies of Amyloid Fibril Structure. *Annu. Rev. Phys. Chem.* **2011**, *62* (1), 279−299.
(40) Reddy, G. N. M.; Huqi, A.; Iuga, D.; Sakurai, S.; Marsh, A.; Davis, J. T.; Masiero, S.; Brown, S. P. Coexistence of Distinct Supramolecular Assemblies in Solution and in the Solid State. *Chem. - Eur. J.* **2017**, *23* (10), 2235.
(41) Cochran, J. E.; Junk, M. J. N.; Glaudell, A. M.; Miller, P. L.; Cowart, J. S.; Toney, M. F.; Hawker, C. J.; Chmelka, B. F.; Chabinyc, M. L. Molecular Interactions and Ordering in Electrically Doped Polymers: Blends of PBTTT and F_4TCNQ. *Macromolecules* **2014**, *47* (19), 6836−6846.
(42) Do, K.; Saleem, Q.; Ravva, M. K.; Cruciani, F.; Kan, Z.; Wolf, J.; Hansen, M. R.; Beaujuge, P. M.; Brédas, J. L. Impact of Fluorine Substituents on π-Conjugated Polymer Main-Chain Conformations, Packing, and Electronic Couplings. *Adv. Mater.* **2016**, *28* (37), 8197−8205.
(43) Melnyk, A.; Junk, M. J. N.; McGehee, M. D.; Chmelka, B. F.; Hansen, M. R.; Andrienko, D. Macroscopic Structural Compositions of π-Conjugated Polymers: Combined Insights from Solid-State NMR and Molecular Dynamics Simulations. *J. Phys. Chem. Lett.* **2017**, *8* (17), 4155−4160.
(44) Nieuwendaal, R. C.; Ro, H. W.; Germack, D. S.; Kline, R. J.; Toney, M. F.; Chan, C. K.; Agrawal, A.; Gundlach, D.; VanderHart, D. L.; Delongchamp, D. M. Measuring Domain Sizes and Compositional Heterogeneities in P3HT-PCBM Bulk Heterojunction Thin Films with 1H Spin Diffusion NMR Spectroscopy. *Adv. Funct. Mater.* **2012**, *22* (6), 1255−1266.
(45) Nieuwendaal, R. C.; DeLongchamp, D. M.; Richter, L. J.; Snyder, C. R.; Jones, R. L.; Engmann, S.; Herzing, A.; Heeney, M.; Fei, Z.; Sieval, A. B.; Hummelen, J. C. Characterization of Interfacial Structure in Polymer-Fullerene Bulk Heterojunctions via 13C{2H} Rotational Echo Double Resonance NMR. *Phys. Rev. Lett.* **2018**, *121* (2), 026101.
(46) Malik, S.; Nandi, A. K. Crystallization Mechanism of Regioregular Poly(3-Alkyl Thiophene)S. *J. Polym. Sci., Part B: Polym. Phys.* **2002**, *40* (18), 2073−2085.
(47) Causin, V.; Marega, C.; Marigo, A.; Valentini, L.; Kenny, J. M. Crystallization and Melting Behavior of Poly(3-Butylthiophene), Poly(3-Octylthiophene), and Poly(3-Dodecylthiophene). *Macromolecules* **2005**, *38* (2), 409−415.
(48) Brouwer, D. H.; Cadars, S.; Eckert, J.; Liu, Z.; Terasaki, O.; Chmelka, B. F. A General Protocol for Determining the Structures of Molecularly Ordered but Noncrystalline Silicate Frameworks. *J. Am. Chem. Soc.* **2013**, *135* (15), 5641−5655.
(49) Sun, H.; Zhong, C.; Brédas, J.-L. Reliable Prediction with Tuned Range-Separated Functionals of the Singlet−Triplet Gap in Organic Emitters for Thermally Activated Delayed Fluorescence. *J. Chem. Theory Comput.* **2015**, *11* (8), 3851−3858.
(50) Sun, H.; Ryno, S.; Zhong, C.; Ravva, M. K.; Sun, Z.; Körzdörfer, T.; Brédas, J.-L. Ionization Energies, Electron Affinities, and Polarization Energies of Organic Molecular Crystals: Quantitative Estimations from a Polarizable Continuum Model (PCM)-Tuned Range-Separated Density Functional Approach. *J. Chem. Theory Comput.* **2016**, *12* (6), 2906−2916.
(51) Takano, Y.; Houk, K. N. Benchmarking the Conductor-like Polarizable Continuum Model (CPCM) for Aqueous Solvation Free Energies of Neutral and Ionic Organic Molecules. *J. Chem. Theory Comput.* **2005**, *1* (1), 70−77.
(52) Lodewyk, M. W.; Siebert, M. R.; Tantillo, D. J. Computational Prediction of ^{1}H and ^{13}C Chemical Shifts: A Useful Tool for Natural Product, Mechanistic, and Synthetic Organic Chemistry. *Chem. Rev.* **2012**, *112*, 1839−1862.
(53) Pierens, G. K. 1H and 13C NMR Scaling Factors for the Calculation of Chemical Shifts in Commonly Used Solvents Using Density Functional Theory. *J. Comput. Chem.* **2014**, *35* (18), 1388−1394.
(54) Benassi, E. Benchmarking of Density Functionals for a Soft but Accurate Prediction and Assignment Of1H And13C NMR Chemical Shifts in Organic and Biological Molecules. *J. Comput. Chem.* **2017**, *38* (2), 87−92.
(55) Konstantinov, I. A.; Broadbelt, L. J. Regression Formulas for Density Functional Theory Calculated1H And13C NMR Chemical Shifts in Toluene- D8. *J. Phys. Chem. A* **2011**, *115* (44), 12364−12372.
(56) Hansen, M. R.; Graf, R.; Sekharan, S.; Sebastiani, D. Columnar Packing Motifs of Functionalized Perylene Derivatives: Local Molecular Order Despite Long-Range Disorder. *J. Am. Chem. Soc.* **2009**, *131* (14), 5251−5256.

DOI: 10.1021/jacs.8b13200
J. Am. Chem. Soc. 2019, 141, 5078−5082

Direct Observation of the Relationship Between Molecular Topology and Bulk Morphology for a π-Conjugated Material

Martin T. Seifrid[†], G. N. Manjunatha Reddy[‡], Cheng Zhou[†], Bradley F. Chmelka[‡]*, Guillermo C. Bazan[†]*

[†]Center for Polymers and Organic Solids, Department of Chemistry and Biochemistry, University of California, Santa Barbara, California, 93106, United States

[‡]Department of Chemical Engineering, University of California, Santa Barbara, California, 93106, United States

Electronic Supplementary Information

Materials and methods

UV-visible absorption spectroscopy: UV-vis absorption spectra were recorded on a Perkin Elmer Lambda 750 UV-Vis spectrometer. The solution spectrum was determined by dissolving TT in chloroform at 0.01 mg/mL. Thin film absorbance measurements were performed using glass as the substrate, and the material was spin coated for 60 s at 1500 rpm at 10 mg/mL in chloroform. Absorbance measurements of the ordered solid and amorphous state were performed at ~ 115 ºC and after quickly cooling to room temperature from ~ 135 ºC. Thin film heating was accomplished by using a heated sample mount. The temperature was measured with an external thermocouple probe.

Solution-state NMR spectroscopy*:* Solution-state ^{1}H and ^{13}C NMR were used to characterize TT. Approximately 10 mg of TT dissolved in 1,1,2,2-tetrachloroethane-d_2 and transferred into a 4 mm NMR tube. All NMR experiments were carried out at room temperature on a Bruker 18.8 T AVANCE-II NMR spectrometer (^{1}H and ^{13}C Larmor frequencies were 800.24 MHz and 200 MHz, respectively) equipped with 4 mm B-B-O probe. The ^{1}H and ^{13}C 90° pulse lengths were of 11 μs and 9 μs, respectively. One-dimensional (1D) ^{1}H NMR spectrum was acquired by co-adding 8 transients using a relaxation delay of 2 s. 1D ^{13}C NMR spectrum was acquired by co-adding1024 transients using a relaxation delay of 2 s corresponding to an experimental time of 1h. WALTZ-16 heteronuclear decoupling[1] was used during the acquisition of ^{13}C spectrum with ^{1}H 180° pulse duration of 60 μs. To identify and distinguish *J*-mediated through-bond ^{1}H-^{1}H and ^{1}H-^{13}C moieties, two-dimensional (2D) ^{1}H{^{1}H} correlation (COSY) and 2D ^{1}H{^{13}C} heteronuclear multiple-bond correlation (HMBC) NMR spectra were acquired and analyzed. 2D ^{1}H{^{1}H} spectrum was acquired using 128 t_1 increments using an incremental time of 114 μs, each by co-adding 2 transients, with a recycle delay of 2 s corresponding to an experimental time of 16 mins. 2D ^{1}H{^{13}C} HMBC spectra were acquired using 3.4 ms ($1/2J_{CH}$, where, J_{CH} = 145 Hz) and 250 ms (i.e., $1/2J_{CH}$, where, J_{CH} = 2 Hz) mixing times, each using 76 t_1 increments with an incremental time of 14.6 μs and by the co-addition of 96 transients with a recycle delay of 2 s corresponding to a total experimental time of 7 h. All ^{1}H and ^{13}C experimental shifts are calibrated with respect to ^{1}H and ^{13}C signals of 1,1,2,2-tetrachloroethane-d_2 at 6.0 and 73.8 ppm, respectively.

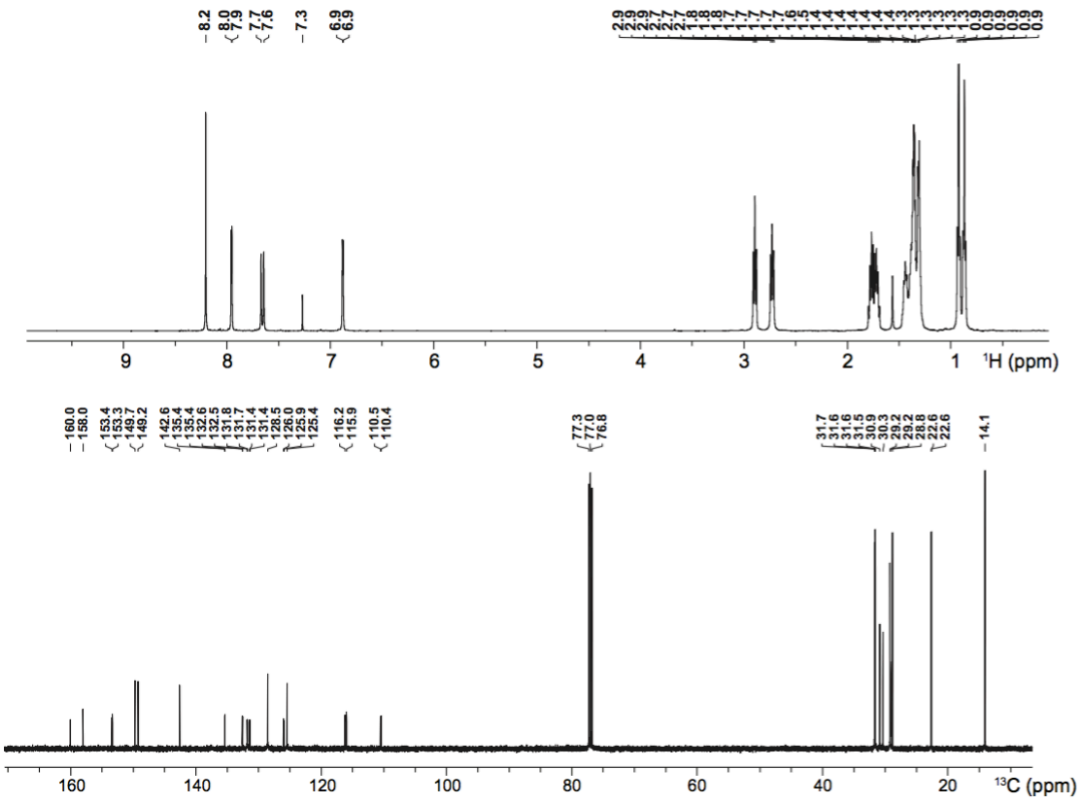

Figure S1. Solution-state ^{1}H and ^{13}C NMR spectra of TT dissolved in 1,1,2,2-tetrachloroethane-d_2 acquired at 18.8 T (^{1}H 800 MHz) at room temperature.

Solution-state ^{1}H and ^{13}C chemical shifts and splittings for the backbone moieties of TT are listed below.

^{1}H solution-state NMR in 1,1,2,2-tetrachloroethane-d_2 (ppm):
8.26 (s, 2H), 8.05 (d, J=3.2 Hz, 2H), 7.77 (d, J=12.9 Hz, 2H), 6.97 (d, J=2.9 Hz, 2H)
^{13}C solution-state NMR in 1,1,2,2-tetrachloroethane-d_2, δ (ppm):
159.2, 153.5, 149.9, 149.7, 142.9, 135.4, 132.7, 132.0, 131.5, 129.0, 126.2, 125.8, 116.3, 110.5

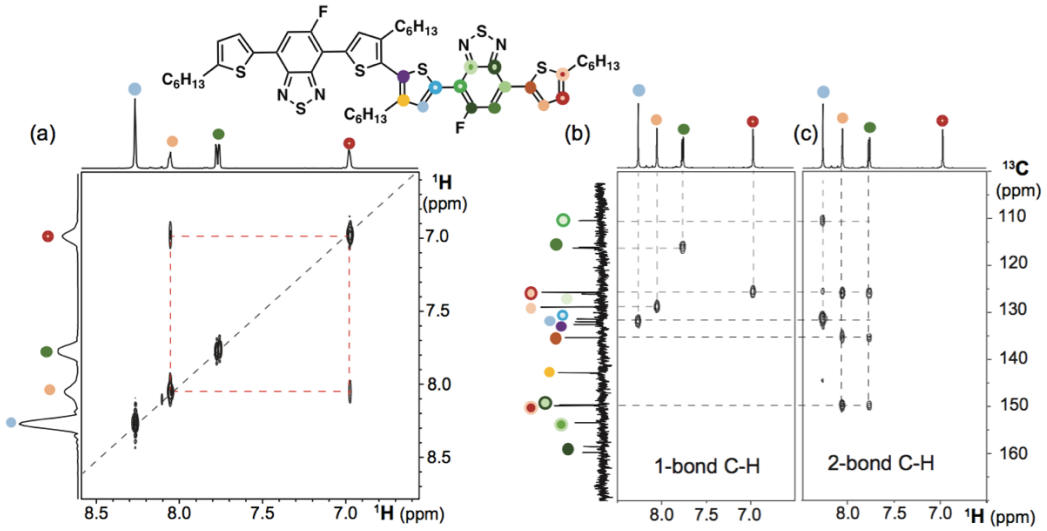

Figure S2. Solution-state 2D $^{1}H\{^{1}H\}$ correlation (COSY) spectrum of TT dissolved in 1,1,2,2-tetrachloroethane-d_2 acquired at 18.8 T (^{1}H 800 MHz) at room temperature. Off diagonal correlation intensities shown in dashed red lines depict the through-bond interactions between thiophene protons.

Solid-state MAS NMR spectroscopy*:* A powder of TT was packed into a 4 mm (outer diameter) zirconia rotor fitted with Teflon insert and a ceramic cap fitted with a rubber *o*-ring to ensure close fitting of the sample. All variable temperature 1D and 2D MAS NMR spectra of TT were acquired on a 11.7 T Bruker AVANCE-II NMR spectrometer equipped with 4 mm H-X-Y probehead and Bruker VT control unit to regulate probe temperature. The ^{1}H and ^{13}C 90º pulse durations were 2.5 µs and 4.0 µs, respectively. To ensure the melt state of TT, single-pulse ^{13}C NMR spectrum was acquired at 135 ºC under a static condition by co-adding 2048 transients using a relaxation delay of 2 s corresponding to an experimental time of 2 h. For TT in the solid state, 1D $^{13}C\{^{1}H\}$ CP-MAS spectra were acquired at 118 ºC using 0.1 ms and 2 ms of CP contact times under 8 kHz MAS conditions using a stream of N_2 gas. Cross polarization involves the simultaneous excitation of ^{1}H and ^{13}C nuclei to enhance the signals of the latter. Heteronuclear decoupling was applied during acquisition of ^{13}C spectra using SPINAL64 sequence[2] using 2048 co-added transients with a 3 s recycle delay, corresponding to an experimental time of 2 h each. To characterize spatially proximate dipole-dipole coupled ^{1}H-^{13}C pairs, 2D $^{13}C\{^{1}H\}$ heteronuclear correlation (HETCOR) NMR spectra were acquired using a short (0.1 ms) and long (2 ms) CP contact times. 2D $^{13}C\{^{1}H\}$ HETCOR NMR spectra were acquired using 32 t_1 increments using an incremental time of 80 µs, each by co-adding 256 transients with a relaxation delay of 3 s corresponding to an experimental time of 7 h each.

All ^{1}H and ^{13}C experimental shifts are calibrated with respect to neat TMS using adamantane as an external reference (higher ppm ^{13}C resonance, 35.8 ppm[3] and the ^{1}H resonance, 1.85 ppm[4]).

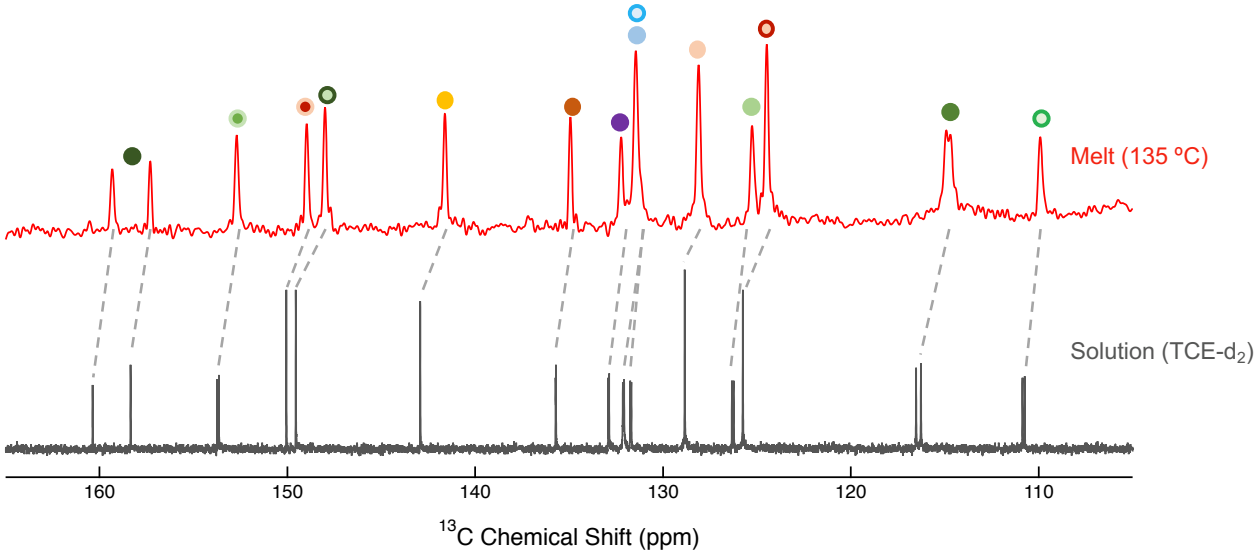

Figure S3. Comparison of single-pulse ^{13}C NMR spectrum of TT acquired at 135 ºC (melt) and the analogous ^{13}C NMR spectrum of TT dissolved in 1,1,2,2-tetrachloroethane-d_2 acquired at room temperature.

Aromatic ^{13}C chemical shifts of TT measured at 135 ºC (melt) and at 118 ºC (ordered solid) are given below.

^{13}C NMR in the melt (135 ºC), δ (ppm):
159.4, 157.4, 152.8, 149.1, 148.1, 141.7, 135.0, 132.3, 131.5, 131.5, 128.2, 125.3, 124.6, 114.9, 110.0
^{13}C solid-state NMR of the solid (118 ºC), δ (ppm):
159.2, 157.6, 154.2, 150.9, 147.6, 139.8, 139.8, 134.3, 132.6, 132.6, 129.7, 123.8, 123.8, 115.4, 110.4

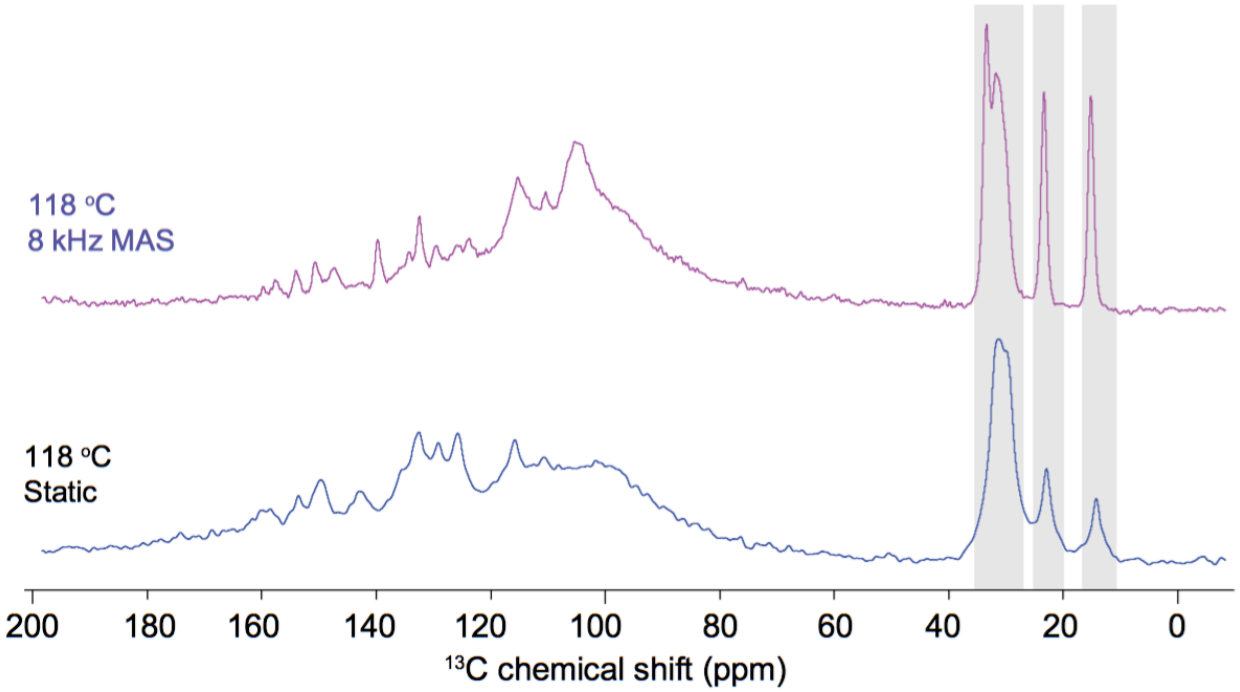

Figure S4. Solid-state single-pulse ^{13}C NMR spectra of TT acquired at 11.7 T and 118 ºC using MAS (top) and static (bottom) conditions. Shaded regions highlight similarities in signal intensities and line widths and suggest the presence of disordered alkyl side chains, whereas the broad spectral features observed in the aromatic region (110 – 160 ppm) of the spectrum acquired under static conditions suggest well ordered, π-π stacked TT backbones.

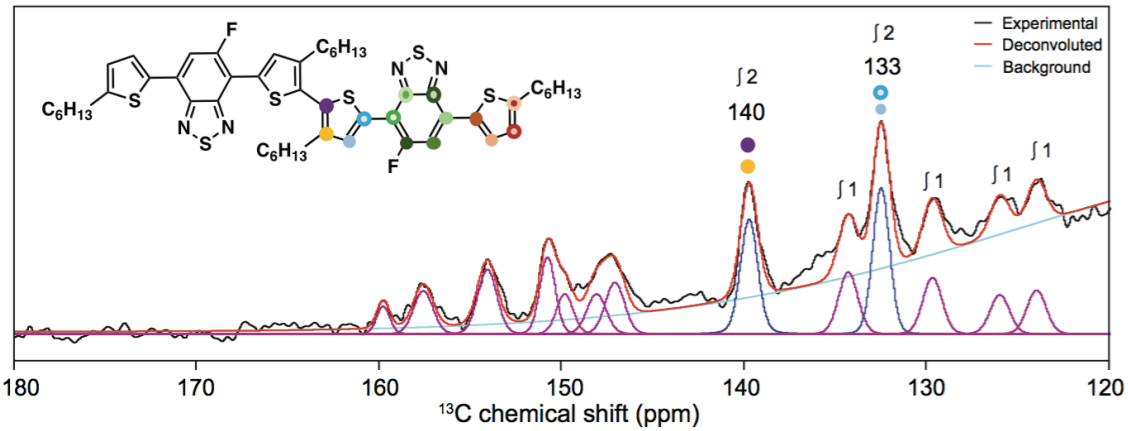

Figure S5. Solid-state single-pulse ^{13}C NMR spectrum of TT acquired at 11.7 T and 118 ºC using high-power ^{1}H-decoupling. Integrals measured from the deconvolution of the spectrum reveal that the signals at 140 and 133 ppm are the overlapping contributions from two different carbon signals.

For TT in the lamellar state at 118 ºC, the local structures of the central and peripheral thiophene groups are elucidated by analyzing 2D $^{13}C\{^{1}H\}$ HETCOR NMR spectra (Figure S6); in the spectrum acquired using 0.1 ms CP contact time, correlated signal intensities at 134 ppm (^{13}C) and 7.6 ppm (^{1}H) correspond to directly bonded ^{13}C-^{1}H of central thiophene (blue dot), and at 130 ppm (^{13}C) and 7.4 ppm (^{1}H) and 115 ppm (^{13}C) and 6.9 ppm (^{1}H) indicate the directly bonded ^{13}C-^{1}H in fluorobenzothiadiazole and thiophene end groups, respectively. In the 2D $^{13}C\{^{1}H\}$ HETCOR NMR

spectrum acquired using 2 ms of CP contact time, correlation intensities originate from thiophene ^{13}C and alkyl sidechain ^{1}H moieties are observed as depicted by dashed horizontal and vertical lines in Figure S6b.

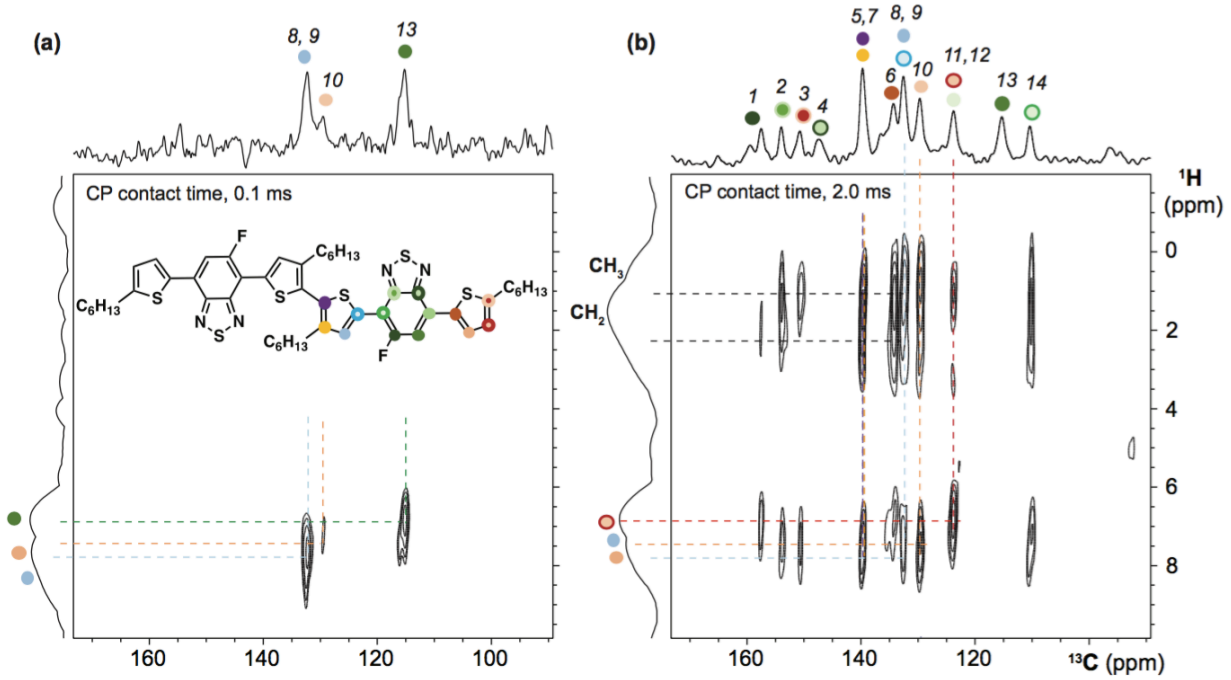

Figure S6. Solid-state 2D $^{13}C\{^{1}H\}$ HETCOR NMR spectrum recorded at 11.7 T and at 118 ºC using (a) 0.1 ms and (b) 2 ms of CP contact times, respectively.

DFT calculations: All calculations were performed using the Gaussian 09 software package.[5] The B3LYP functional and 6-31G(d,p) basis set were used to optimize the ground-state equilibrium geometry of TT. For the planar conformation, the central S-C-C-S dihedral was frozen at 180º and the rest of the structure was allowed to optimize the ground-state equilibrium geometry. The twisted conformation of TT was allowed to relax to the lowest energy conformation without any constraints. For each conformer of TT, the range-separation parameter ω in the ωB97XD functional was tuned using the gap tuning procedure.[6] The structures were subsequently optimized to their ground-state equilibrium geometries using the tuned ωB97XD/6-31G(d,p) functional and basis set by the same methods described above; ω = 0.1253 $bohr^{-1}$ for the twisted conformer and ω = 0.1081 $bohr^{-1}$ for the trans-planar conformer. These optimized geometries were used to calculate magnetic shieldings using the gauge-independent atomic orbital (GIAO) method in a conductor-like polarizable continuum model (CPCM)[7] for a conjugated organic material (where the static dielectric constant is set to ε = 3.5 and the dynamic dielectric constant is set to $\varepsilon_{inf} = 2$)[8] with the tuned ωB97XD functional and 6-311+G(2d,p) basis set. Plots of experimental ^{13}C chemical shifts versus GIAO DFT-calculated NMR chemical shifts are shown in Figure S7 for the planar and twisted TT conformations.

Based on calculations of different possible rota-mers for both the twisted and planar confor-mations of TT, planarization of the molecule may also involve a flip of the fluorobenzothiadiazole (FBT) heterocycles and outer thiophene rings. This additional reconfiguration is reasonable, as single crystal data for similar compounds have shown a multitude of rotamer populations.[9–11]

Computationally predicted chemical shieldings, σ_{iso}, can be compared to experimental isotropic chemical shifts, δ_{iso}, by using the following conversion,[12–17]

$$\delta_{iso} = \frac{intercept - \sigma_{iso}}{-slope} \quad (1)$$

where *intercept* and *slope* are the intercept and slope determined from linear regression analysis in Figure S7.

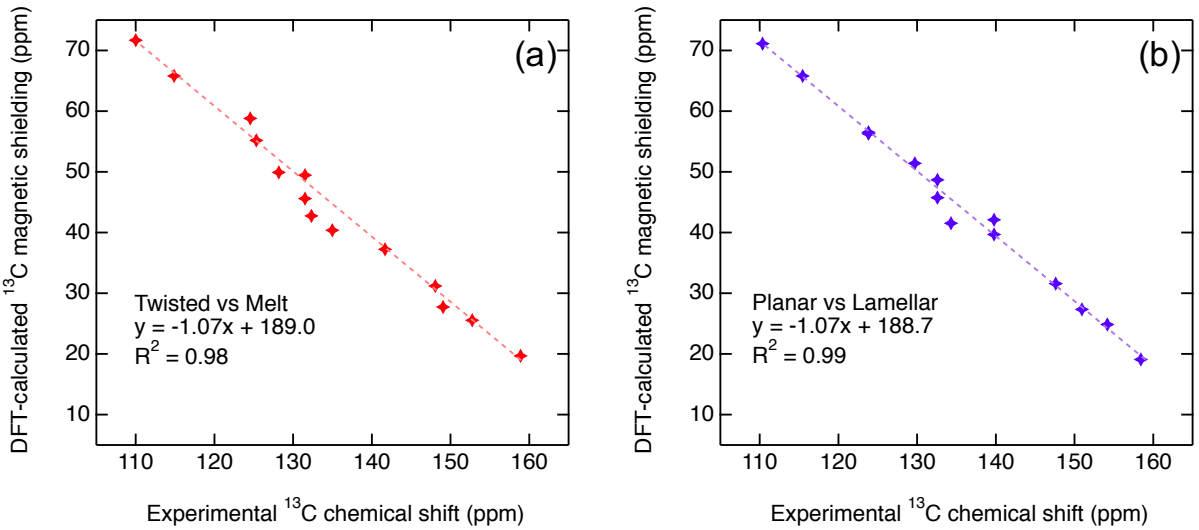

Figure S7. Plots of DFT-calculated ^{13}C chemical shieldings versus experimental ^{13}C chemical shifts obtained for the twisted (a) and planar (b) conformations of TT models from the high-temperature ^{13}C NMR spectra acquired at 135 ºC and 118 ºC, respectively. Regression analyses are presented in figure insets, which depict reasonably good agreements with R^2 values 0.98 and 0.99 for the twisted and planar conformers of TT, respectively.

DFT-calculated isotropic ^{13}C chemical shieldings for the backbone carbon atoms of TT are given below.

Twisted conformer, σ_{iso} (ppm):
19.6941, 25.5663, 27.7351, 31.2094, 37.257, 40.3939, 42.7596, 45.6088, 49.4673, 49.9177, 55.1814, 58.8164, 65.7932, 71.682
Planar conformer, σ_{iso} (ppm):
19.1113, 24.8516, 27.3565, 31.6064, 39.6791, 41.5304, 42.1121, 45.7494, 48.6781, 51.4214, 56.2908, 56.5454, 65.8058, 71.1200

References

(1) Shaka, A. J.; Keeler, J.; Frenkiel, T.; Freeman, R. An Improved Sequence for Broadband Decoupling: WALTZ-16. *J. Magn. Reson. 1969* **1983**, *52* (2), 335–338.

(2) Khitrin, A.; Fung, B. M. Design of Heteronuclear Decoupling Sequences for Solids. *J. Chem. Phys.* **2000**, *112* (5), 2392–2398.

(3) Morcombe, C. R.; Zilm, K. W. Chemical Shift Referencing in MAS Solid State NMR. *J. Magn. Reson.* **2003**, *162* (2), 479–486.

(4) Hayashi, S.; Hayamizu, K. Chemical-Shift Standards in High-Resolution Solid-State Nmr (1) 13C, 29Si and 1H Nuclei. *Bull. Chem. Soc. Jpn.* The Chemical Society of Japan 公益社団法人 日本化学会 February 7, 1991, pp 685–687.

(5) Frisch, M. J.; Trucks, G. W.; Schlegel, H. B.; Scuseria, G. E.; Robb, M. A.; Cheeseman, J. R.; Scalmani, G.; Barone, V.; Mennucci, B.; Petersson, G. A.; Nakatsuji, H.; Caricato, M.; Li, X.; Hratchian, H. P.; Izmaylov, A. F.; Bloino, J.; Zheng, G.; Sonnenberg, J. L.; Hada, M.; Ehara, M.; Toyota, K.; Fukuda, R.; Hasegawa, J.; Ishida, M.; Nakajima, T.; Honda, Y.; Kitao, O.; Nakai, H.; Vreven, T.; Montgomery, J. A.; Peralta, J. E.;

Ogliaro, F.; Bearpark, M.; Heyd, J. J.; Brothers, E.; Kudin, K. N.; Staroverov, V. N.; Keith, T.; Kobayashi, R.; Normand, J.; Raghavachari, K.; Rendell, A.; Burant, J. C.; Iyengar, S. S.; Tomasi, J.; Cossi, M.; Rega, N.; Millam, J. M.; Klene, M.; Knox, J. E.; Cross, J. B.; Bakken, V.; Adamo, C.; Jaramillo, J.; Gomperts, R.; Stratmann, R. E.; Yazyev, O.; Austin, A. J.; Cammi, R.; Pomelli, C.; Ochterski, J. W.; Martin, R. L.; Morokuma, K.; Zakrzewski, V. G.; Voth, G. A.; Salvador, P.; Dannenberg, J. J.; Dapprich, S.; Daniels, A. D.; Farkas, O.; Foresman, J. B.; Ortiz, J. V.; Cioslowski, J.; Fox, D. J. Gaussian 09, Revision D.01. Gaussian, Inc.: Wallingford, CT 2016.

(6) Sun, H.; Zhong, C.; Brédas, J.-L. Reliable Prediction with Tuned Range-Separated Functionals of the Singlet–Triplet Gap in Organic Emitters for Thermally Activated Delayed Fluorescence. *J. Chem. Theory Comput.* **2015**, *11* (8), 3851–3858.

(7) Takano, Y.; Houk, K. N. Benchmarking the Conductor-like Polarizable Continuum Model (CPCM) for Aqueous Solvation Free Energies of Neutral and Ionic Organic Molecules. *J. Chem. Theory Comput.* **2005**, *1* (1), 70–77.

(8) Sun, H.; Ryno, S.; Zhong, C.; Ravva, M. K.; Sun, Z.; Körzdörfer, T.; Brédas, J.-L. Ionization Energies, Electron Affinities, and Polarization Energies of Organic Molecular Crystals: Quantitative Estimations from a Polarizable Continuum Model (PCM)-Tuned Range-Separated Density Functional Approach. *J. Chem. Theory Comput.* **2016**, *12* (6), 2906–2916.

(9) Van Der Poll, T. S.; Zhugayevych, A.; Chertkov, E.; Bakus, R. C.; Coughlin, J. E.; Teat, S. J.; Bazan, G. C.; Tretiak, S. Polymorphism of Crystalline Molecular Donors for Solution-Processed Organic Photovoltaics. *J. Phys. Chem. Lett.* **2014**, *5* (15), 2700–2704.

(10) Coughlin, J. E.; Zhugayevych, A.; Bakus, R. C.; van der Poll, T. S.; Welch, G. C.; Teat, S. J.; Bazan, G. C.; Tretiak, S. A Combined Experimental and Theoretical Study of Conformational Preferences of Molecular Semiconductors. *J. Phys. Chem. C* **2014**, *118* (29), 140627161810001.

(11) McDowell, C.; Narayanaswamy, K.; Yadagiri, B.; Gayathri, T.; Seifrid, M.; Datt, R.; Ryno, S. M.; Heifner, M. C.; Gupta, V.; Risko, C.; Singh, S. P.; Bazan, G. C. Impact of Rotamer Diversity on the Self-Assembly of Nearly Isostructural Molecular Semiconductors. *J. Mater. Chem. A* **2018**, *6* (2), 383–394.

(12) Lodewyk, M. W.; Siebert, M. R.; Tantillo, D. J. Computational Prediction of ^{1}H and ^{13}C Chemical Shifts: A Useful Tool for Natural Product, Mechanistic, and Synthetic Organic Chemistry. *Chem. Rev.* **2012**, *112* (3), 1839–1862.

(13) Pierens, G. K. ^{1}H and ^{13}C NMR Scaling Factors for the Calculation of Chemical Shifts in Commonly Used Solvents Using Density Functional Theory. *J. Comput. Chem.* **2014**, *35* (18), 1388–1394.

(14) Benassi, E. Benchmarking of Density Functionals for a Soft but Accurate Prediction and Assignment of ^{1}H and ^{13}C NMR Chemical Shifts in Organic and Biological Molecules. *J. Comput. Chem.* **2017**, *38* (2), 87–92.

(15) Konstantinov, I. A.; Broadbelt, L. J. Regression Formulas for Density Functional Theory Calculated ^{1}H and ^{13}C NMR Chemical Shifts in Toluene- d_8. *J. Phys. Chem. A* **2011**, *115* (44), 12364–12372.

(16) Reddy, G. N. N. M.; Cook, D. S.; Iuga, D.; Walton, R. I.; Marsh, A.; Brown, S. P. An NMR Crystallography Study of the Hemihydrate of 2′, 3′-O-Isopropylidineguanosine. *Solid State Nucl. Magn. Reson.* **2015**, *65*, 41–48.

(17) Reddy, G. N. M.; Marsh, A.; Davis, J. T.; Masiero, S.; Brown, S. P. Interplay of Noncovalent Interactions in Ribbon-like Guanosine Self-Assembly: An NMR Crystallography Study. *Cryst. Growth Des.* **2015**, *15* (12), 5945–5954.